ACS APPLIED POLYMER MATERIALS

pubs.acs.org/acsapm Article

Can the Voigt Model be Directly Used for Determining the Modulus of Graphene in Laminate Thin Films?

Zacary L. Croft, Zhen Xu, Ke Cao, Dong Guo, Saran Sreeharikesan, Connor Thompson, Gabriel Zeltzer,* and Guoliang Liu*

Cite This: *ACS Appl. Polym. Mater.* 2022, 4, 394−402 Read Online

ACCESS | Metrics & More | Article Recommendations | Supporting Information

ABSTRACT: Laminate thin-film composites that couple polymers with single-layer graphene (SLG) are lightweight and have shown superb electromechanical strength. The mechanical strengths of the composites can be described by elastic micromechanical models such as the Voigt mixing rule. However, the reinforcement behavior between polymer and SLG has raised questions about the validity of such models in laminate composites at the nanoscale. Herein, we have fabricated laminate thin films of poly(ether imide) and SLG (PEI/SLG) with varying volume fractions of SLG (ϕ_g) as a model system to evaluate the effective reinforcement using the mixing rule. Linear regression analysis of the Young's modulus of the composite (E_c) versus ϕ_g revealed an unexpectedly high-effective Young's modulus of large-area, polycrystalline SLG, E_g = 1.12 ± 0.05 TPa. Further analysis of theoretical and experimental E_c using the Voigt−Poisson model showed a lower maximum value of $E_g \sim 0.9$ TPa for films with $\phi_g \geq 0.11$ vol %. Our results show that an ideal mixing rule is followed only beyond a critical value of ϕ_g for laminate thin-film composites, which explains the wide inconsistency of E_g reported in the literature. This knowledge will guide the fabrication of laminate polymer−graphene thin films with near-ideal mechanical reinforcement.

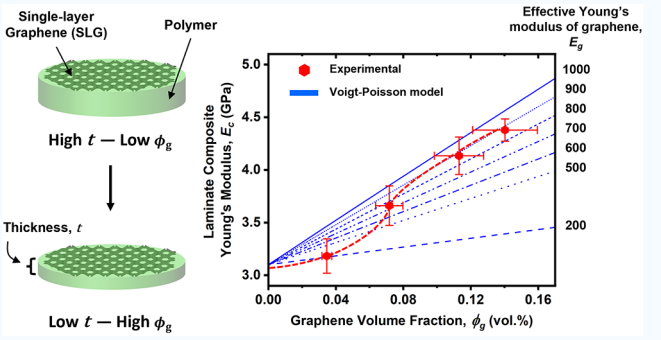

KEYWORDS: *graphene, thin-films, laminates, polymer composites, mechanical reinforcement*

1. INTRODUCTION

Free-standing, low-dimensional nanocomposites show substantial promise in next-generation flexible electronics, such as wearable sensors and actuators,[1−3] roll-up displays,[4] and bendable solar cells.[5−8] Graphene, having exceptional mechanical, electrical, thermal, and chemical properties, is a perfect building block for constructing free-standing, low-dimensional nanocomposites.[9−14] In particular, single-layer graphene (SLG) prepared via chemical vapor deposition provides high electrical conductivity over arbitrarily large areas,[15] which is required for high-performance micro- and nanoelectromechanical systems (MEMS/NEMS). However, SLG is often polycrystalline and prone to fracture, thus requiring a structural support to be freely suspended over large areas, especially when the lateral dimension is over several hundred micrometers.[16] Construction of polymer/graphene laminates that are composed of two or more continuous constituent layers can potentially address this challenge. The polymer layer protects SLG from fracture, and SLG maintains its beneficial electrical properties for MEMS and NEMS applications.[1,17−20]

The interaction of polymer and graphene at the matrix−filler interface, defined herein as the "polymer/graphene interface", is directly responsible for the properties of the resulting composites. The lamination of atomically thin graphene with polymer creates a matrix−filler interface of semi-infinite aspect ratio, which maximizes the mechanical reinforcement of the two components.[21] Furthermore, because all atoms of graphene are surface atoms, the effective properties of graphene will depend on its interaction with the polymer. However, despite its significance in laminate systems, the exact physiochemical nature of the polymer/graphene interface and the effect of this interface on the composite properties is still not well-understood.

One method for investigating the polymer/graphene interface is to examine the effective Young's modulus of graphene in laminate composites. Most commonly, the Voigt upper bound mixing rule is employed to model the effective Young's modulus of the composite (E_c) due to its simplicity. Mathematically, the Voigt mixing rule takes the general form,

Received: October 4, 2021
Accepted: December 6, 2021
Published: December 21, 2021

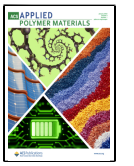

https://doi.org/10.1021/acsapm.1c01328
ACS Appl. Polym. Mater. 2022, 4, 394−402

$$E_c = E_g\phi_g + E_p\phi_p \quad (1)$$

where E and ϕ are the effective Young's modulus and volume fraction, respectively, of graphene (g) and polymer (p) and ϕ is related to the thickness (t); for instance, $\phi_g = \frac{t_g}{t_g + t_p}$. Compared with the widely accepted Young's modulus of pristine graphene established by nanoindentation ($E_g \sim 1.0$ TPa),[22] a wide range of lower values (0.36−0.91 TPa) have been reported for various polymer/graphene laminates by simply extracting the E_g value using the Voigt model,[21,23−25] raising questions about the validity of simply using Voigt model to extract Young's modulus of its components in laminate composites.

The reduction of the effective E_g in polymer/graphene laminates could be potentially attributed to process-related structural defects (e.g., point and line defects, static wrinkling) in CVD-derived SLG, but the large variability in the effective E_g of laminate composites cannot be simply explained as the result of defects. For example, Berger et al.[23] found $E_g = 0.75 \pm 0.10$ TPa by regression analysis of E_c vs ϕ_g in bilayer laminates of parylene-C/SLG with ϕ_g in the range 0.16−1.5 vol %, and the extrapolated E_g was 44% larger than that measured for bare SLG using the same method (measured $E_g = 0.52 \pm 0.16$ TPa). Wang et al.[25] reported $E_g = 0.64$−0.91 TPa for ∼100 nm-thick bilayer laminates of polycarbonate/SLG with $\phi_g \sim 0.34$ vol %, and the E_g values varied depending on the polycrystallinity of SLG and loading direction. Liu et al.[21] found that, when the same material was stacked to form alternating multilayers of polycarbonate/SLG, a much lower effective E_g of ∼0.36 TPa was extracted. Considering the substantial discrepancies of E_g in the literature, careful investigation of the polymer/graphene interface and the applicability of Voigt model to the laminate composites are required.

We hypothesize that polymer/graphene laminate composites may not have ideal mixing at submicron thicknesses due to the complex nature of the polymer/graphene interface. Instead, these composites will likely exhibit ideal mixing behavior at and above some critical value of ϕ_g when the two materials are close enough to fully interact with each other. To test our hypothesis, we fabricated bilayer poly(ether imide) (PEI)/SLG thin films of submicron thickness ($t = 0.23$−0.97 μm) to investigate the variability of effective E_g in laminate composites. We have chosen PEI because of its high mechanical strength ($E_p \sim 3$ GPa) and expect that its aromatic nature provides good interfacial stress transfer with SLG and maximizes the structural reinforcement. By varying the thickness of PEI, we tune the volume fraction of SLG in the laminate films and thus vary the contribution of the polymer/graphene interface to the effective mechanical strength of the composite. The Voigt mixing rule is then used to linearly model the effective E_g of PEI/SLG, which reveals an overestimation of E_g. Further comparison of theoretical and experimental E_c values shows the nonlinear behavior of E_g and demonstrates that a maximum value of E_g is achieved past a critical value of ϕ_g.

2. EXPERIMENTAL SECTION

2.1. Synthesis of Single-Layer Graphene. Single-layer graphene (SLG) was grown via atmospheric pressure chemical vapor deposition (APCVD) on 25 μm-thick Cu foil (Alfa Aesar). Prior to APCVD, Cu foils were electropolished following a previous report.[26] APCVD consisted of four stages: preannealing, annealing, growth, and cooling. In preannealing, the Cu foils were placed in a quartz tube reaction chamber, which was purged with Ar three times. Then, the Cu foils were heated to 1045 °C in 30 min in a tube furnace under an Ar flow of 250 sccm (standard cubic centimeters per minute). Next, the Cu foils were annealed at 1045 °C for 30 min under 250 sccm Ar and 30 sccm H_2. Graphene growth was performed at 1045 °C for 10 min under a mixture of 2 sccm CH_4, 250 sccm Ar, and 30 sccm H_2. After 10 min, CH_4 and H_2 flows were stopped, and then, the foils were rapidly cooled to room temperature under 250 sccm Ar after removing them from the heating zone.

2.2. Laminate PEI/SLG Thin-Film Fabrication. Bilayer thin films of poly(ether imide) and single-layer graphene (PEI/SLG) were fabricated by spin-coating PEI solutions at 3000 rpm for 1 min over SLG on Cu using a Laurell WS-650MZ spin-coater. The concentrations of PEI solutions were 3, 4, 5, and 6 wt/v% in $CHCl_3$ (e.g., 6 wt/v% means 6 g of PEI in 100 mL of $CHCl_3$). The as-spun films were predried in air for ∼2 h before annealing at 270 °C for 12 h in a vacuum oven (MTI Corp.).

2.3. Transfer of PEI/SLG Thin Films. PEI/SLG was prepared for dynamic mechanical analysis (DMA) following the camphor-enabled transfer method developed by Wang et al.[24] To deposit camphor, the laminate stack of PEI/SLG/Cu was fastened to a glass dish and inverted over a beaker filled with solid camphor (∼2−3 g). Heating at 160 °C for ∼1 h sublimed most of the solid camphor, which then solidified on PEI/SLG/Cu due to the temperature difference between the top and bottom of the beaker. Afterward, Cu was removed by wet-chemical etching in $(NH_4)_2S_2O_8$ (APS-100, Transcene Inc.) with subsequent cleaning first in RCA base solution ($H_2O/H_2O_2/NH_4OH$ = 5:1:1 by volume) and then RCA acid solution ($H_2O/H_2O_2/H_2SO_4$ = 5:1:1 by volume). The films were cleaned in both solutions for 5 min each, with water rinsing for 2 min in between and after cleaning. The films were then dried before being transferred and adhered to a new substrate.

2.4. Profilometry. PEI/SLG film thickness was measured using a stylus profilometer (Dektak 150, Veeco) in contact-scan mode. Prior to profilometry, films were transferred to Si/SiO_2 (<1 nm surface roughness) using the camphor-mediated method described above. Adhesion to Si/SiO_2 was aided by the addition of 1−4 water droplets between the film and substrate, followed by heating at ∼50 °C for ∼1 h to gradually evaporate water and adhere PEI/SLG to the substrate. A minimum of five profile measurements were collected for each PEI/SLG film, and each PEI/SLG profile was evaluated to determine the average film thickness (t) and root-mean-squared surface roughness (R_q) using Dektak v.9.3 surface analysis software.

2.5. Mechanical Analysis and Modeling. The tensile response of PEI/SLG was tested under uniaxial tension using a Q800 dynamic mechanical analyzer (TA Instruments) in controlled stress−strain mode (ASTM D638). PEI/SLG was first cut into "dog-bones" and then transferred using the camphor-mediated method described above. Upon loading, both sides of the transfer support were cut away to free the film (Figure S1). Each film was visually examined for cracks and tears prior to testing, and only films without structural abnormalities were tested mechanically. Tensile tests were performed isothermally at 30 °C using a controlled force ramp rate of 0.4 N min^{-1} and 0.001 N preload force to monitor the resulting strain (ε). The engineering stress (σ) experienced by a film under uniaxial tension is,

$$\sigma = \frac{F_{app}}{A} = \frac{F_{app}}{t \times w} \quad (2)$$

where F_{app} is the applied force and A is the cross-sectional area of the film (= thickness, t × width, w). E_c values were determined by fitting the linear elastic region of $\sigma \sim \varepsilon$.

To evaluate the mechanical mixing behavior of PEI/SLG quantitatively, the linear form of the Voigt upper bound mixing equation was applied considering $\phi_p + \phi_g = 1$,

$$E_c = (E_g - E_p)\phi_g + E_p \quad (3)$$

where the effective composite modulus (E_c) is a volume weighted sum of the effective Young's moduli of SLG (E_g) and poly(ether imide) (E_p). Experimental E_c values determined from the tensile testing of

https://doi.org/10.1021/acsapm.1c01328
ACS Appl. Polym. Mater. 2022, 4, 394−402

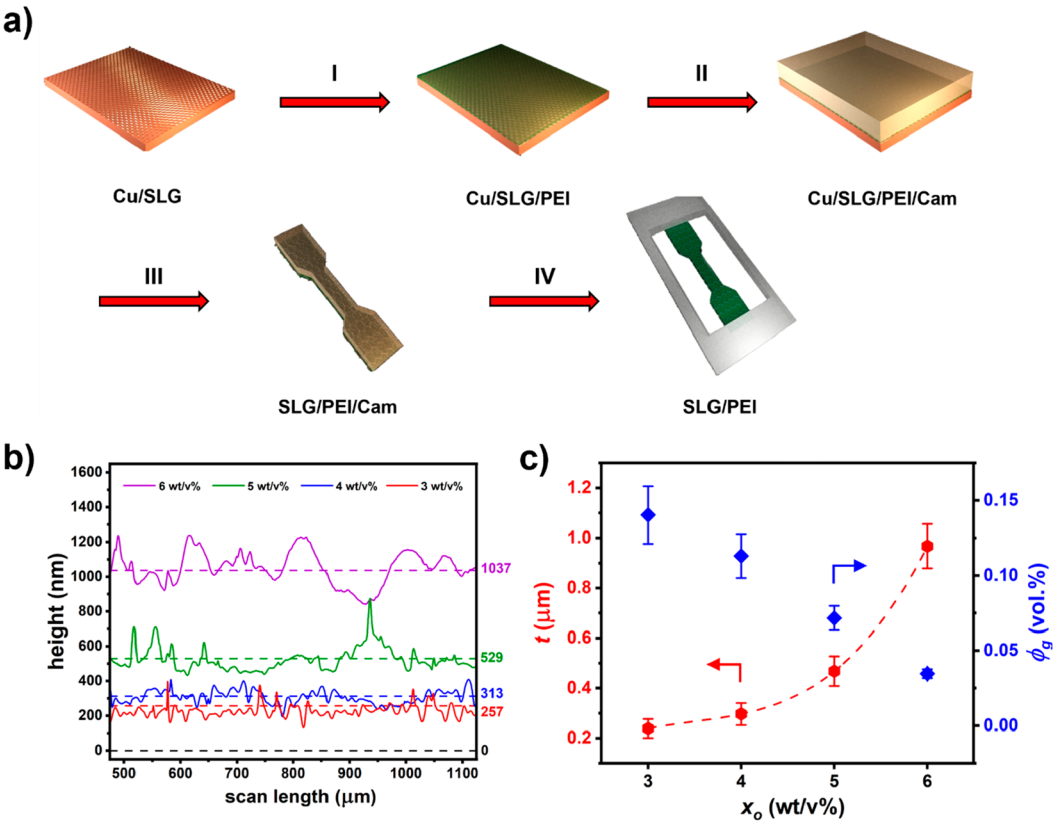

Figure 1. Fabrication and characterization of PEI/SLG laminate thin films. (a) Scheme for PEI/SLG fabrication. (I) PEI (green) is spin-coated on SLG/Cu (illustrated as a honeycomb structure on an orange substrate), followed by thermal annealing at 280 °C for 12 h. (II) Camphor (cam, beige) is deposited on PEI/SLG at 160 °C for 20 min. (III) Cam/PEI/SLG/Cu is cut into "dog-bones" (ASTM D638). (IV) Cu is etched away using $(NH_4)_2S_2O_8$; Cam/PEI/SLG is cleaned, dried, and transferred to a hollow transfer support; sublimation of camphor at ambient temperature overnight yields PEI/SLG suspended on the transfer support. (b) Representative height profiles of PEI/SLG fabricated using PEI solutions at concentrations of 3, 4, 5, and 6 wt/v%. (c) Average thickness (t) and volume fraction of SLG (ϕ_g) as a function of initial PEI solution concentration (x_o).

PEI/SLG were plotted as a function of ϕ_g, and the effective modulus of SLG (E_g) was determined from the linear regression analysis of $E_c \sim \phi_g$ based on eq 2.

The thermo-viscoelastic mechanical behavior of PEI/SLG was evaluated by temperature-sweep thermomechanical analysis using a dynamic mechanical analyzer (Q800 DMA, TA Instruments) in tension mode (ASTM D5026). The storage modulus (E') and loss modulus (E'') of PEI/SLG were monitored across a temperature range of 90−270 °C while subjecting films to a dynamic, oscillatory strain (1 Hz frequency, 15 μm amplitude) and heating at a rate of 3 °C/min. The glass transition temperature (T_g) at varying ϕ_g was determined by monitoring E' and E'' of PEI/SLG in the glassy-to-rubbery transition. From the profiles of $E' \sim T$ and $E'' \sim T$, T_g was determined from the onset drop in E' and peak of E'' in the transition regime, respectively. The damping factor ($\tan \delta$) was ill-defined in all thermomechanical measurements of PEI/SLG and was therefore not used to determine T_g. Mean values of T_g were determined using multiple measurements of $E' \sim T$ and $E'' \sim T$ to establish a statistical relationship between T_g and ϕ_g.

The Voigt−Poisson model was also used to evaluate the theoretical mechanical mixing behavior of PEI/SLG. The Voigt−Poisson equation is given by,[27]

$$E_c = E_g\phi_g + E_p\phi_p + \frac{\phi_g\phi_p E_g E_p(\nu_g - \nu_p)^2}{E_p\phi_p(1-\nu_g^2) + E_g\phi_g(1-\nu_p^2)} \quad (4)$$

where ν is Poisson's ratio. Theoretical curves of $E_c(\phi_g)$ were obtained using eq 4 and selected E_p, ν_g, and ν_p values of 3.1 GPa, 0.15, and 0.44, respectively, while varying values of E_g in the range 200−1000 GPa. Experimental and theoretical E_c values were plotted together as a function of ϕ_g to compare the $E_c \sim \phi_g$ trend observed experimentally with that predicted by the Voigt−Poisson model using eq 4.

3. RESULTS AND DISCUSSION

3.1. Fabrication, Transfer, and Thickness. Laminate polymer/graphene thin films consisted of poly(ether imide) (PEI) and large-area single-layer graphene (SLG) and were prepared by spin-coating PEI solution over SLG on Cu (Figure 1a, I). The SLG was grown on Cu foil by atmospheric-pressure CVD and was a polycrystalline, as confirmed by Raman spectroscopy (Figure S1). Camphor-mediated transfer of nanoscale thin films was used previously by Wang et al. to improve the results of mechanical analysis and prevent the introduction of transfer-related structural defects.[24] Therefore, we used the camphor-mediated method to transfer PEI/SLG to Si/SiO_2 for profile measurements and hollow structural supports for mechanical analysis (Figure 1a, II). The mean thickness of a camphor layer deposited on PEI/SLG was 300 μm (~300 times thicker than PEI/SLG), which greatly helped preserve the structural integrity of PEI/SLG during transfer.

The SLG volume fraction (ϕ_g) is given by $\phi_g = t_g/t$ for laminate SLG-based thin films, where t_g is the thickness of graphene and t is total film thickness.[23,28] Assuming an effective SLG thickness (t_g) of ~0.335 nm, ϕ_g is subsequently determined by measuring t. Because t depends on the initial polymer concentration (x_o) during spin-coating,[29] solutions of

https://doi.org/10.1021/acsapm.1c01328
ACS Appl. Polym. Mater. 2022, 4, 394−402

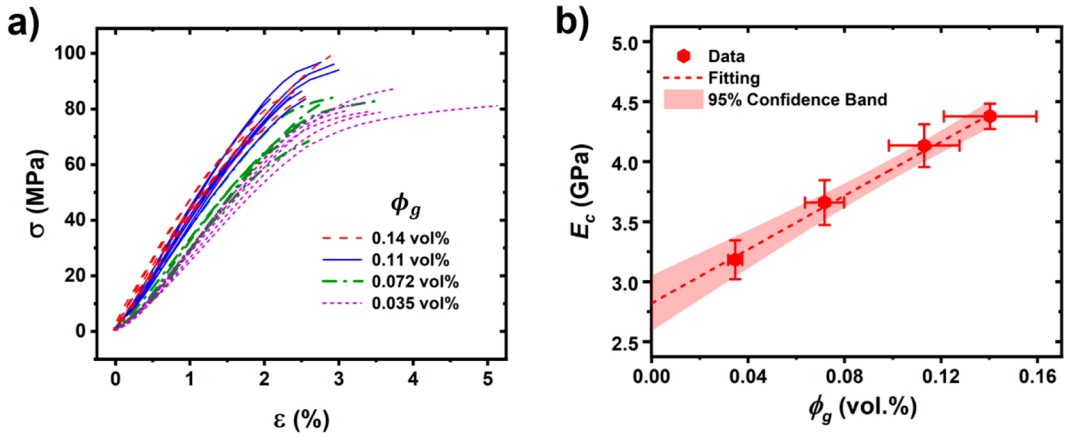

Figure 2. (a) Representative tensile curves of PEI/SLG at varying ϕ_g. (b) Average E_c of PEI/SLG as a function of ϕ_g. Fitting (GPa): $E_c = 1120\phi_g + 2.81$; $R^2 = 0.995$.

varying x_o = 3, 4, 5, and 6 wt/v% afforded control over t and thus ϕ_g. The x_o values were calculated using $x_o = m_{PEI}/V_{sol}$, where m_{PEI} is the mass of PEI in grams and V_{sol} is the solvent volume in milliliters.

Contact-based, stylus profilometry was used to produce height profiles and determine the mean t of PEI/SLG films produced using PEI solutions of differing x_o values (Figure 1b). The mean value of t increased with x_o and was 0.24 ± 0.04, 0.30 ± 0.04, 0.47 ± 0.06, and 0.97 ± 0.08 μm for 3, 4, 5, and 6 wt/v% PEI, respectively (Figure 1c). The thinnest successfully transferred PEI/SLG without breakage was ∼0.24 μm, slightly thicker than the 100 nm-thick polycarbonate/SLG thin films reported by Wang et al.[24] The observed trend between thickness and concentration was non-linear, suggesting that hydrodynamic thinning behavior dominates the film formation process.[29] Therefore, a third-order, empirical fitting of $t \sim x_o$ was employed to model the thickness trend mathematically. The root-mean-squared surface roughness (R_q) of the films provided the most reasonable values for the uncertainty of t, and the magnitude of R_q increased with x_o, further illustrating the importance of hydrodynamics. The corresponding ϕ_g values equaled 0.14 ± 0.02, 0.11 ± 0.01, 0.072 ± 0.008, and 0.035 ± 0.003 vol % for 3, 4, 5, and 6 wt/v% PEI/SLG, respectively.

3.2. Mechanical Analysis. Tensile testing elucidated the mechanical mixing behavior of PEI/SLG by providing the effective composite Young's modulus (E_c) at varying ϕ_g. To preserve film integrity, the camphor-mediated method was employed to transfer and load films into a dynamic mechanical analyzer (Figure 1a, III). The camphor-mediated transfer greatly improved the transferability of PEI/SLG and helped provide reproducible tensile responses by preserving film structure during the transfer process (Figure S2). Once removed from Cu, PEI/SLG with a camphor coating was transferred and adhered to a hollow support frame to prevent scrolling or folding of the films. After sublimation of camphor, PEI/SLG suspended on the hollow frame was transferred to a mechanical analyzer, and the edges of the frame were removed after the film was clamped into the instrument. The process resulted in wrinkle free PEI/SLG that yielded uniformly across the film upon tensile tests (Figure S3).

Comparing the tensile curves of PEI/SLG at varying ϕ_g (Figure 2a), the tensile response gradually shifted upward in slope with increasing ϕ_g. Remarkably, E_c increased from 3.2 ± 0.2 to 4.4 ± 0.1 GPa as ϕ_g increased from only 0.035 to 0.14 vol % and as thickness decreased from 0.97 to 0.23 μm. To verify that the observed increase in E_c was not due to nanoscale-thickness-induced stiffening of PEI, thin films of PEI without SLG were fabricated by spin-coating 5 wt/v% PEI on bare Cu foil that had been O_2-plasma treated to remove the SLG layer.

The neat PEI thin films had an average thickness of 0.45 ± 0.02 μm (as measured by profilometry), similar to the thickness of PEI/SLG (0.47 ± 0.06 μm) also fabricated using 5 wt/v% PEI solution. The neat PEI thin films exhibited an average Young's modulus of 3.1 ± 0.2 GPa (Figure S4), which is comparable to bulk PEI (∼3.0 GPa) and markedly lower than 0.47 μm-thick PEI/SLG (E_c = 3.7 ± 0.2 GPa). Additional control measurements were also attempted with neat PEI films fabricated from 3 and 4 wt/v% PEI solution, but despite many attempts, these films repeatedly broke once separated from the Cu substrate. These results suggest that the Young's modulus of the PEI component remains constant at thicknesses ≥0.45 μm and declines as thickness decreases to <0.45 μm. Therefore, we conclude that the steady increase of E_c with ϕ_g (Figure 2a) is unlikely to be caused by nanoscale-induced stiffening of the PEI layer.

Linear regression analysis of $E_c \sim \phi_g$ determined the effective reinforcement of PEI with SLG on the basis of the Voigt mixing model (Figure 2b). The effective Young's modulus of SLG (E_g) determined from the linear regression was 1.12 ± 0.05 TPa, higher than that of pristine graphene reported in the literature (∼1.0 TPa).[13,30,31] Consequently, such a high-effective Young's modulus might be interpreted as an enhancement of the intrinsic modulus of SLG caused by the polymer−graphene interaction. However, the modulus of CVD-derived graphene is known to suffer from structural defects (e.g., grain boundaries, point-defects) that lower the mechanical properties to below that of pristine graphene.[13] Furthermore, E_g determined for PEI/SLG is much larger than that of polycrystalline SLG measured in other polymer/graphene laminate composites previously using the Voigt model (E_g = 0.36−0.91 TPa).[21,23−25] Therefore, the Voigt analysis may not provide an accurate description of the effective mechanical properties, and understanding the limitations of its use will likely require a more thorough evaluation.

https://doi.org/10.1021/acsapm.1c01328
ACS Appl. Polym. Mater. 2022, 4, 394−402

To understand and explain this disparity, we first considered potential thermo-viscoelastic micromechanical changes. For example, Ruoff and co-workers reported substantial mechanical reinforcement seemingly exceeding the Voigt model prediction in thin-film composites of poly(methyl methacrylate)/graphene oxide (PMMA/GO) ($t \sim 0.2$ mm).[10] This abnormal reinforcement behavior was later explained by Li and McKenna,[32] who showed that strong, noncovalent interactions (e.g., hydrogen bonding) induced viscoelastic stiffening. Consequently, the purely elastic model employed by Ruoff overestimated the effective mechanical properties of the GO filler because it did not account for the stiffening of PMMA caused by hydrogen bond formation between OH and ester groups of GO and PMMA, respectively.[32] Considering the structural similarity between PEI/SLG and PMMA/GO films, we investigated the potential changes in viscoelastic micromechanics with respect to thickness to better evaluate the mechanical reinforcement in laminate PEI/SLG thin films.

Viscoelastic micromechanical changes are correlated with shifting glass transition temperature (T_g) of a material.[32] If viscoelastic stiffening occurs, a T_g shift will be observed in the thermomechanical responses of storage modulus (E') and loss modulus (E'') (Figure 3a). The glassy-to-rubbery transition defines T_g of a material and is typically characterized by an abrupt drop in E' and a peak in E''. Although technically PEI is not a rubber, here we use the term "rubbery" state to differentiate it from the glassy state. For PEI/SLG, mechanical failure occurred immediately following the glass transition, indicating that the mechanical stability of PEI in the rubbery state is reduced at submicron thicknesses. Consequently, there were no clearly defined tan δ peaks for our films, and thus, T_g values were determined solely from the responses of E' and E'' within the transition region.

Statistically, there was no discernible difference between the T_g values of PEI/SLG when ϕ_g was in the range 0.035−0.11 vol % (Figure 3b). There was also no statistical difference between the T_g of these PEI/SLG films and bulk PEI control films, indicating that the thermal operating range of bulk PEI is largely preserved in PEI/SLG at thicknesses ≥0.30 μm. The absence of an increase in T_g shows that there is little or no viscoelastic stiffening in PEI/SLG. The absence of a T_g shift with changing ϕ_g can be explained as follows: (i) there are no interactions present for PEI/SLG known to cause viscoelastic stiffening (e.g., hydrogen bonding); (ii) matrix−filler interactions are localized to the interface of PEI and SLG; (iii) the planar structure of graphene offers no interlocking with PEI. Therefore, the reinforcement behavior observed in PEI/SLG cannot stem from thermo-viscoelastic micromechanical changes.

The only significant change in T_g occurred for PEI/SLG with ϕ_g = 0.14 vol % (mean $T_g \sim 206$ °C), which was lower than that of the thicker films. The low T_g was likely due to physical abnormalities during fabrication, transfer, or loading, which reduced the mechanical integrity of PEI/SLG and increased variability in the onset of T_g. The effect is expected to be more pronounced for thinner PEI/SLG films, and our inability to produce intact films less than 0.23 μm supports this assumption. Conversely, the thermomechanical responses of thicker PEI/SLG films were more reproducible and regular, suggesting that structural irregularities become less significant for PEI/SLG films with thicknesses over 0.23 μm.

Thermomechanical analysis provided additional information about the reinforcement behavior of PEI/SLG, elucidating

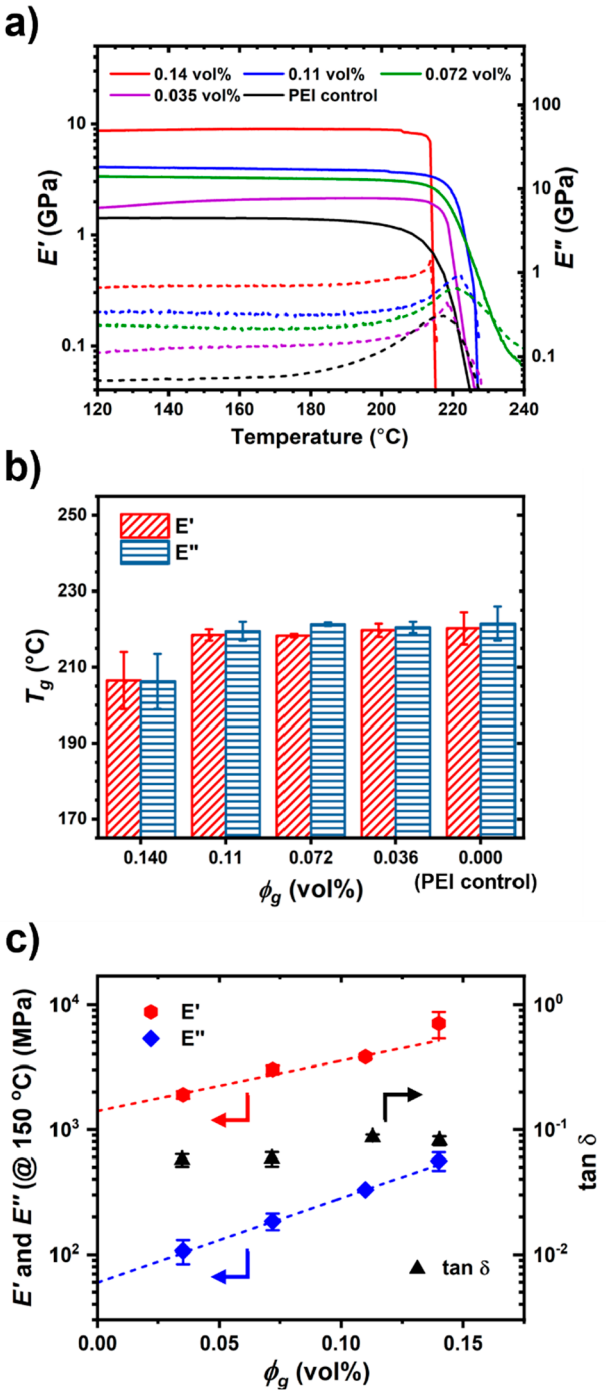

Figure 3. Thermomechanics of PEI/SLG. (a) Storage modulus (E', solid) and loss modulus (E'', dashed) vs temperature. (b) Bar graph depicting mean T_g of PEI/SLG with error bars as a function of ϕ_g. (c) E' (red), E'' (blue), and tan δ (black) at 150 °C vs ϕ_g. Fitting equations: $\log(E') = 4.02\ \phi_g + 3.15$, $R^2 = 0.963$; $\log(E'') = 6.74\ \phi_g + 1.78$, $R^2 = 0.996$.

changes in E' and E'' as a function of ϕ_g (Figure 3c). PEI/SLG experienced increased E' and E'' with increasing ϕ_g (decreasing t) across the measured temperature range. The E' values for PEI/SLG at 150 °C with ϕ_g = 0.035, 0.072, 0.11, and 0.14 vol % were 46%, 132%, 194%, and 442% greater than those of bulk PEI, respectively. Additionally, the E'' values at 150 °C were 42%, 144%, 338%, and 649% greater, respectively. Notably, the

https://doi.org/10.1021/acsapm.1c01328
ACS Appl. Polym. Mater. 2022, 4, 394−402

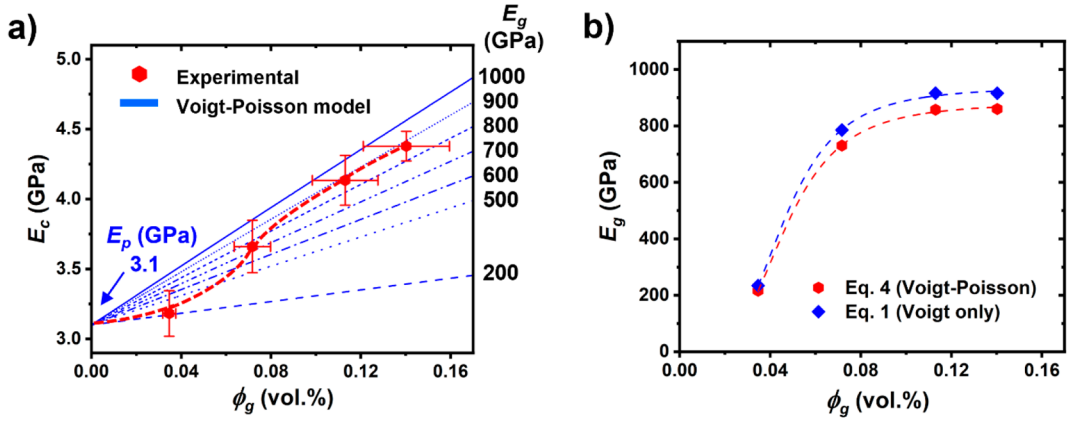

Figure 4. (a) Comparison of the experimentally measured E_c of PEI/SLG with theoretical prediction bands calculated using the Voigt−Poisson model (eq 4). E_p = 3.1 GPa (measured); E_g = 200−1000 GPa; ν_p = 0.44; ν_g = 0.15. The red dashed line is a guide to the eye, showing the trend approximates to the Voigt−Poisson model as ϕ_g increases. (b) Effective E_g of PEI/SLG, derived from experimental E_c values using the Voigt−Poisson and standard Voigt models, plotted as a function of ϕ_g.

increases in both E' and E'' closely followed a logarithmic trend rather than a linear one that was predicted by the Voigt model. The deviation of reinforcement behavior from linearity is observable by the poor fit of E' and E'' by linear regression (Figure S5) and was most pronounced for the thinnest PEI/SLG films (ϕ_g = 0.14 vol %). We believe that this deviation further demonstrates the inadequacy of the Voigt mixing model in predicting the reinforcement behavior. Overall, the reinforcement trend of E' and E'' shows that as thickness decreases and ϕ_g increases, (i) the effective elastic modulus of PEI/SLG is improved (i.e., E' increases), meaning thinner PEI/SLG films are better at storing and releasing energy elastically; (ii) thinner PEI/SLG films also dissipate energy more effectively (i.e., E'' increases), possibly because of larger surface-to-volume ratios.

Another important dynamic mechanical parameter, the loss or damping factor (tan δ), is defined as the ratio of E'' to E'. The tan δ was analyzed across a temperature range of 100−200 °C (below T_g) to determine mean values for PEI/SLG films of varying thickness (and ϕ_g) and evaluate potential differences in damping behavior (Figure 3c). While some fluctuation in tan δ was observed across the measured temperature range (Figure S6), the standard deviations of mean values, however, were ≤1%, suggesting that the fluctuations were insignificant. Overall, we found no clear trend for the change in tan δ with ϕ_g.

3.3. Mechanical Modeling. Because the standard Voigt mixing model (eq 1) does not account for the potential contributions of Poisson effect to mechanical stiffening, an additional term is introduced to account for such contributions to the mechanical stiffening of a composite (eq 4). This modified form of the standard Voigt equation is known as the "Voigt−Poisson model", and the additional term represents "Poison stiffening". The standard Voigt model assumes ideal mechanical mixing and perfect stress transfer between matrix and filler, so the unusually high-effective E_g of PEI/SLG suggests that mechanical mixing between PEI and SLG may include Poisson stiffening, which would be misrepresented by the Voigt model as an increase in the intrinsic mechanical properties of SLG. Assuming very effective mechanical mixing between PEI and SLG (supported by the large E_g), any additional Poisson stiffening would likely enhance the apparent mechanical strength of PEI/SLG beyond the upper limit of the standard Voigt model. Therefore, the extent to which Poisson stiffening contributes to the effective reinforcement of PEI/SLG demands an in-depth analysis.

According to eq 4, Poisson stiffening is expected to contribute to E_c most significantly when the Poisson's ratios (ν) differ the most between matrix and filler. The Poisson ratio of PEI (ν_p) is reported to be in the range ∼0.36−0.44,[33−36] and that of graphene (ν_g) exhibits a much wider range (∼0.15−0.45).[31] We chose 0.44 and 0.15 for ν_p and ν_g, respectively, to maximize the Poisson's ratio difference between PEI and SLG and to evaluate the greatest potential contributions of Poisson stiffening.

Comparison of experimentally determined E_c values with theoretical E_c bands calculated using the Voigt−Poisson model provides a semiempirical method of evaluating the accuracy and validity of our experimental measurements. For this comparison, we plotted multiple $E_c \sim \phi_g$ curves predicted by the Voigt−Poisson model (eq 4) at various effective E_g values using the measured value of E_p (3.1 GPa) provided by tensile experiments on neat PEI thin-film controls (Figure 4a). Across the ϕ_g range investigated, the reinforcement trend does not conform to any single prediction of the Voigt−Poisson model. Interestingly, there appears to be lower effective E_g at a lower ϕ_g, which cannot be explained by the Voigt−Poisson model. An effective E_g of PEI/SLG was derived from experimental E_c measurements using eq 4, which yielded values of ∼220, 744, 872, and 875 GPa for ϕ_g= 0.14, 0.11, 0.072, and 0.035 vol %, respectively.

Effective E_g values extracted from the Voigt model both with and without consideration of Poisson stiffening (eqs 4 and 1, respectively) were plotted against ϕ_g to illustrate the variability of E_g at the submicron scale (Figure 4b). The effective E_g of PEI/SLG substantially increases for ϕ_g > 0.035 vol % and plateaus when ϕ_g reaches 0.11 vol %. In other words, the composite Young's modulus E_c normally falls below both the Voigt and Voigt−Poisson models and approximates these models when ϕ_g reaches a sufficiently large value or the polymer layer becomes sufficiently thin ($\phi_g \geq$ 0.11 vol % and $t \leq$ 300 nm in this work, Figure 4a). Thus, the E_g values determined from the Voigt model with and without considering Poisson stiffening were 881 and 938 GPa, respectively. The difference between E_g values established by the Voigt−Poisson and standard Voigt models was 57 GPa

https://doi.org/10.1021/acsapm.1c01328
ACS Appl. Polym. Mater. 2022, 4, 394−402

(~6%−7%), which signifies the maximum error expected from neglecting the Poisson effect. Nevertheless, our result shows clearly that the effective E_g can vary substantially with the thickness of PEI/SLG going from the submicron to nanoscale. However, the variation is not likely caused by Poisson stiffening.

The E_g in our PEI/SLG thin films (881−938 GPa) is at the upper end of the E_g range expected for CVD-derived SLG yet below the E_g of pristine graphene. In the literature, a wide range of values for free-standing, polycrystalline SLG suspended on Si/SiO_2 has been reported between 0.16 and 0.98 TPa.[22,37] The mechanical strength of free-standing graphene has been shown to suffer from point defects,[38] out-of-plane flexural phonons, and static wrinkling,[39] especially for CVD-grown polycrystalline graphene.[37,40] We did not perform any special procedures to maximize the grain sizes or cleanliness of SLG, so it is interesting to find such a high-effective E_g here, even with Poisson effects considered. One possible reason for such a high maximum E_g value is that the mechanical strength of graphene is reinforced by PEI. Because SLG conforms to the topology of a substrate closely, more so than multilayer graphene, the conformity minimizes the interplanar distance between SLG and PEI and maximizes noncovalent binding interactions, such as van der Waals (vdWs) forces. The strong vdWs forces between SLG and PEI can help suppress the out-of-plane flexural phonons and static wrinkling, which are detrimental to the mechanical strength of polycrystalline SLG. Additionally, DFT calculations have shown that binding between SLG and polymer greatly lowers the surface energy of graphene, especially at reactive defect sites,[41] which likely helps to preserve the mechanical properties of graphene further.

On the basis of the above analysis, it becomes clear that the mixing model must be employed cautiously when determining the effective E_g in laminate composites, particularly for mutually reinforced polymer and SLG in bilayer structures. Berger et al.[23] used Voigt analysis in their study of parylene-C/SLG composites and found an effective E_g greater than that directly measured using both nanoindentation and microblister techniques (Figure S7).[23] Consequently, in both Berger and our study, the Voigt approximation seems to be invalid for modeling the mechanical mixing of laminate polymer/graphene composites.

The reinforcement behavior exhibited by these composites, both for Berger and in our study, does not appear to always follow the Voigt mixing model, suggesting that perfect stress transfer is achieved only for certain values of ϕ_g. For PEI/SLG, the point at which near-perfect stress transfer appears to be achieved is above a critical ϕ_g of ~0.11 vol %. Past this point, the Voigt model seems to be an accurate description of mechanical reinforcement. However, the reason for why PEI/SLG does not follow the Voigt model below the critical point of ϕ_g remains unclear. To answer this question, additional consideration would need to be given to the factors influencing stress transfer at the interface of SLG and polymer when evaluating mechanical reinforcement in laminate composites, factors not apparent from mechanical measurements alone. Therefore, future studies of polymer/graphene laminate composites should seek to correlate the physiochemical characteristics of the polymer/graphene interface with the observed mechanical reinforcement of polymer with graphene to uncover the fundamental origins of the mechanical mixing behavior.

4. CONCLUSIONS

We have demonstrated the fabrication of laminate PEI/SLG thin films of submicron thicknesses ranging from 0.97 to 0.23 μm, corresponding to volume fractions of SLG from 0.035 to 0.14 vol %. Mechanical tensile testing of PEI/SLG initially appeared to reveal an effective SLG Young's modulus of 1.12 ± 0.05 TPa but was overestimated by linear regression analysis using the standard Voigt mechanical mixing model. Thermo-mechanical analysis showed no observable correlation between T_g and ϕ_g, thereby ruling out the possibility of viscoelastic stiffening contributions to the modulus of PEI/SLG. Comparison of the theoretical predictions of the Voigt mixing model and experimental results illustrated that the effective SLG Young's modulus changed significantly with ϕ_g and plateaued at a critical value of $\phi_g \sim 0.11$ vol %. This result implies that the mechanical reinforcement is more effective for thinner laminate films and that the mechanical properties of laminate composites could approach the Voigt mixing upper bound as the thicknesses of the constituent layers decrease. Future studies should seek to answer how physiochemical changes at the interface of polymer and graphene affect the mechanical properties of polymer−graphene laminates.

■ ASSOCIATED CONTENT

Supporting Information

The Supporting Information is available free of charge at https://pubs.acs.org/doi/10.1021/acsapm.1c01328.

Figures of Raman spectra, photographs of camphor deposition, optical photographs of PEI/SLG thin films clamped in a Q800 dynamic mechanical analyzer, tensile curves, storage modulus (E') and loss modulus (E'') as a function of SLG volume fraction, representative curves of the mechanical loss factor vs temperature, and effective Young's modulus as a function of ϕ_g and discussion of Voigt mechanical modeling by linear regression (PDF)

■ AUTHOR INFORMATION

Corresponding Authors

Gabriel Zeltzer − *Waves Audio Ltd., Tel-Aviv 6701101, Israel*; Email: gabrielz@waves.com

Guoliang Liu − *Department of Chemistry, Virginia Tech, Blacksburg, Virginia 24061, United States; Macromolecules Innovation Institute and Division of Nanoscience, Academy of Integrated Science, Virginia Tech, Blacksburg, Virginia 24061, United States;* orcid.org/0000-0002-6778-0625; Email: gliu1@vt.edu

Authors

Zacary L. Croft − *Department of Chemistry, Virginia Tech, Blacksburg, Virginia 24061, United States*

Zhen Xu − *Department of Chemistry, Virginia Tech, Blacksburg, Virginia 24061, United States*

Ke Cao − *Macromolecules Innovation Institute, Virginia Tech, Blacksburg, Virginia 24061, United States;* orcid.org/0000-0001-7204-7455

Dong Guo − *Department of Chemistry, Virginia Tech, Blacksburg, Virginia 24061, United States;* orcid.org/0000-0002-3469-2602

Saran Sreeharikesan − *Division of Nanoscience, Academy of Integrated Science, Virginia Tech, Blacksburg, Virginia 24061, United States*

https://doi.org/10.1021/acsapm.1c01328
ACS Appl. Polym. Mater. 2022, 4, 394−402

Connor Thompson − *Division of Nanoscience, Academy of Integrated Science, Virginia Tech, Blacksburg, Virginia 24061, United States*

Complete contact information is available at: https://pubs.acs.org/10.1021/acsapm.1c01328

Notes

The authors declare no competing financial interest.

■ ACKNOWLEDGMENTS

The authors acknowledge use of facilities within the Nanoscale Characterization and Fabrication Laboratory (NCFL) in the Institute for Critical Technology and Applied Science (ICTAS) at Virginia Tech (VT). The authors also thank the Associate Dean and Professor of Physics, Dr. Randy Heflin, for generously allowing us to use his equipment and laboratory space for experiments during this study. This material is based upon work partially supported by Waves Audio Ltd. and the National Science Foundation under grant no. DMR-1752611.

■ REFERENCES

(1) Khan, A. U.; Zeltzer, G.; Speyer, G.; Croft, Z. L.; Guo, Y.; Nagar, Y.; Artel, V.; Levi, A.; Stern, C.; Naveh, D.; Liu, G. Mutually Reinforced Polymer−Graphene Bilayer Membranes for Energy-Efficient Acoustic Transduction. *Adv. Mater.* **2021**, *33* (2), 2004053.

(2) Taccola, S.; Greco, F.; Zucca, A.; Innocenti, C.; de Julián Fernández, C.; Campo, G.; Sangregorio, C.; Mazzolai, B.; Mattoli, V. Characterization of Free-Standing PEDOT:PSS/Iron Oxide Nanoparticle Composite Thin Films and Application As Conformable Humidity Sensors. *ACS Appl. Mater. Interfaces* **2013**, *5* (13), 6324−6332.

(3) Abid; Sehrawat, P.; Islam, S. S.; Gulati, P.; Talib, M.; Mishra, P.; Khanuja, M. Development of highly sensitive optical sensor from carbon nanotube-alumina nanocomposite free-standing films: CNTs loading dependence sensor performance Analysis. *Sens. Actuators, A* **2018**, *269*, 62−69.

(4) Chun, K.-Y.; Kim, S. H.; Shin, M. K.; Kim, Y. T.; Spinks, G. M.; Aliev, A. E.; Baughman, R. H.; Kim, S. J. Free-standing nanocomposites with high conductivity and extensibility. *Nanotechnology* **2013**, *24* (16), 165401.

(5) Gao, L.; Chao, L.; Hou, M.; Liang, J.; Chen, Y.; Yu, H.-D.; Huang, W. Flexible, transparent nanocellulose paper-based perovskite solar cells. *npj Flexible Electronics* **2019**, *3* (1), 4.

(6) Li, X.; Li, P.; Wu, Z.; Luo, D.; Yu, H.-Y.; Lu, Z.-H. Review and perspective of materials for flexible solar cells. *Materials Reports: Energy* **2021**, *1* (1), 100001.

(7) Malara, F.; Manca, M.; Lanza, M.; Hübner, C.; Piperopoulos, E.; Gigli, G. A free-standing aligned-carbon-nanotube/nanocomposite foil as an efficient counter electrode for dye solar cells. *Energy Environ. Sci.* **2012**, *5* (8), 8377−8383.

(8) Zhu, R.; Zhang, Z.; Li, Y. Advanced materials for flexible solar cell applications. *Nanotechnol. Rev.* **2019**, *8* (1), 452−458.

(9) Xie, T.; Wang, Q.; Wallace, R. M.; Gong, C. Understanding and optimization of graphene gas sensors. *Appl. Phys. Lett.* **2021**, *119* (1), 013104.

(10) Potts, J. R.; Dreyer, D. R.; Bielawski, C. W.; Ruoff, R. S. Graphene-based polymer nanocomposites. *Polymer* **2011**, *52* (1), 5−25.

(11) Kim, H.; Abdala, A. A.; Macosko, C. W. Graphene/Polymer Nanocomposites. *Macromolecules* **2010**, *43* (16), 6515−6530.

(12) Young, R. J.; Kinloch, I. A.; Gong, L.; Novoselov, K. S. The mechanics of graphene nanocomposites: A review. *Compos. Sci. Technol.* **2012**, *72* (12), 1459−1476.

(13) Papageorgiou, D. G.; Kinloch, I. A.; Young, R. J. Mechanical properties of graphene and graphene-based nanocomposites. *Prog. Mater. Sci.* **2017**, *90*, 75−127.

(14) Ferrari, A. C.; Bonaccorso, F.; Fal'ko, V.; Novoselov, K. S.; Roche, S.; Bøggild, P.; Borini, S.; Koppens, F. H. L.; Palermo, V.; Pugno, N.; Garrido, J. A.; Sordan, R.; Bianco, A.; Ballerini, L.; Prato, M.; Lidorikis, E.; Kivioja, J.; Marinelli, C.; Ryhänen, T.; Morpurgo, A.; Coleman, J. N.; Nicolosi, V.; Colombo, L.; Fert, A.; Garcia-Hernandez, M.; Bachtold, A.; Schneider, G. F.; Guinea, F.; Dekker, C.; Barbone, M.; Sun, Z.; Galiotis, C.; Grigorenko, A. N.; Konstantatos, G.; Kis, A.; Katsnelson, M.; Vandersypen, L.; Loiseau, A.; Morandi, V.; Neumaier, D.; Treossi, E.; Pellegrini, V.; Polini, M.; Tredicucci, A.; Williams, G. M.; Hee Hong, B.; Ahn, J.-H.; Min Kim, J.; Zirath, H.; van Wees, B. J.; van der Zant, H.; Occhipinti, L.; Di Matteo, A.; Kinloch, I. A.; Seyller, T.; Quesnel, E.; Feng, X.; Teo, K.; Rupesinghe, N.; Hakonen, P.; Neil, S. R. T.; Tannock, Q.; Löfwander, T.; Kinaret, J. Science and technology roadmap for graphene, related two-dimensional crystals, and hybrid systems. *Nanoscale* **2015**, *7* (11), 4598−4810.

(15) Suk, J. W.; Kitt, A.; Magnuson, C. W.; Hao, Y.; Ahmed, S.; An, J.; Swan, A. K.; Goldberg, B. B.; Ruoff, R. S. Transfer of CVD-Grown Monolayer Graphene onto Arbitrary Substrates. *ACS Nano* **2011**, *5*, 6916.

(16) Afyouni Akbari, S.; Ghafarinia, V.; Larsen, T.; Parmar, M. M.; Villanueva, L. G. Large Suspended Monolayer and Bilayer Graphene Membranes with Diameter up to 750 μm. *Sci. Rep.* **2020**, *10* (1), 6426.

(17) Khan, Z. H.; Kermany, A. R.; Öchsner, A.; Iacopi, F. Mechanical and electromechanical properties of graphene and their potential application in MEMS. *J. Phys. D: Appl. Phys.* **2017**, *50* (5), 053003.

(18) Chen, C.; Rosenblatt, S.; Bolotin, K. I.; Kalb, W.; Kim, P.; Kymissis, I.; Stormer, H. L.; Heinz, T. F.; Hone, J. Performance of monolayer graphene nanomechanical resonators with electrical readout. *Nat. Nanotechnol.* **2009**, *4* (12), 861−867.

(19) Zhou, Q.; Zettl, A. Electrostatic graphene loudspeaker. *Appl. Phys. Lett.* **2013**, *102* (22), 223109.

(20) Huang, Y.; Liang, J.; Chen, Y. The application of graphene based materials for actuators. *J. Mater. Chem.* **2012**, *22* (9), 3671−3679.

(21) Liu, P.; Jin, Z.; Katsukis, G.; Drahushuk, L. W.; Shimizu, S.; Shih, C.-J.; Wetzel, E. D.; Taggart-Scarff, J. K.; Qing, B.; Van Vliet, K. J.; Li, R.; Wardle, B. L.; Strano, M. S. Layered and scrolled nanocomposites with aligned semi-infinite graphene inclusions at the platelet limit. *Science* **2016**, *353* (6297), 364.

(22) Lee, G.-H.; Cooper, R. C.; An, S. J.; Lee, S.; van der Zande, A.; Petrone, N.; Hammerberg, A. G.; Lee, C.; Crawford, B.; Oliver, W.; Kysar, J. W.; Hone, J. High-Strength Chemical-Vapor−Deposited Graphene and Grain Boundaries. *Science* **2013**, *340* (6136), 1073.

(23) Berger, C. N.; Dirschka, M.; Vijayaraghavan, A. Ultra-thin graphene−polymer heterostructure membranes. *Nanoscale* **2016**, *8* (41), 17928−17939.

(24) Wang, B.; Luo, D.; Li, Z.; Kwon, Y.; Wang, M.; Goo, M.; Jin, S.; Huang, M.; Shen, Y.; Shi, H.; Ding, F.; Ruoff, R. S. Camphor-Enabled Transfer and Mechanical Testing of Centimeter-Scale Ultrathin Films. *Adv. Mater.* **2018**, *30* (28), 1800888.

(25) Wang, B.; Li, Z.; Wang, C.; Signetti, S.; Cunning, B. V.; Wu, X.; Huang, Y.; Jiang, Y.; Shi, H.; Ryu, S.; Pugno, N. M.; Ruoff, R. S. Folding Large Graphene-on-Polymer Films Yields Laminated Composites with Enhanced Mechanical Performance. *Adv. Mater.* **2018**, *30* (35), 1707449.

(26) Zhang, B.; Lee, W. H.; Piner, R.; Kholmanov, I.; Wu, Y.; Li, H.; Ji, H.; Ruoff, R. S. Low-Temperature Chemical Vapor Deposition Growth of Graphene from Toluene on Electropolished Copper Foils. *ACS Nano* **2012**, *6* (3), 2471−2476.

(27) Liu, B.; Feng, X.; Zhang, S.-M. The effective Young's modulus of composites beyond the Voigt estimation due to the Poisson effect. *Compos. Sci. Technol.* **2009**, *69* (13), 2198−2204.

(28) Ye, S.; Huang, H.; Yuan, C.; Liu, F.; Zhai, M.; Shi, X.; Qi, C.; Wang, G. Thickness-Dependent Strain Effect on the Deformation of the Graphene-Encapsulated Au Nanoparticles. *J. Nanomater.* **2014**, *2014*, 989672.

(29) Lawrence, C. J. Spin coating with slow evaporation. *Phys. Fluids A* **1990**, *2* (3), 453−456.
(30) Zhong, T.; Li, J.; Zhang, K. A molecular dynamics study of Young's modulus of multilayer graphene. *J. Appl. Phys.* **2019**, *125* (17), 175110.
(31) Cao, G. Atomistic Studies of Mechanical Properties of Graphene. *Polymers* **2014**, *6* (9), 2404−2432.
(32) Li, X.; McKenna, G. B. Considering Viscoelastic Micromechanics for the Reinforcement of Graphene Polymer Nanocomposites. *ACS Macro Lett.* **2012**, *1* (3), 388−391.
(33) Xu, Z.; Gehui, L.; Cao, K.; Guo, D.; Serrano, J.; Esker, A.; Liu, G. Solvent-Resistant Self-Crosslinked Poly(ether imide). *Macromolecules* **2021**, *54* (7), 3405−3412.
(34) Fukuhara, M. Temperature dependency of elastic moduli and internal dilational and shear frictions of polyetherimide. *J. Appl. Polym. Sci.* **2003**, *90* (3), 759−764.
(35) Overview of materials for Polyetherimide (PEI). MatWeb: Materials Property Data.
(36) Professional Plastics. Mechanical Properties of Plastic Materials. https://www.professionalplastics.com/ (accessed December 1, 2021).
(37) Ruiz-Vargas, C. S.; Zhuang, H. L.; Huang, P. Y.; van der Zande, A. M.; Garg, S.; McEuen, P. L.; Muller, D. A.; Hennig, R. G.; Park, J. Softened Elastic Response and Unzipping in Chemical Vapor Deposition Graphene Membranes. *Nano Lett.* **2011**, *11* (6), 2259−2263.
(38) Deng, S.; Berry, V. Wrinkled, rippled and crumpled graphene: an overview of formation mechanism, electronic properties, and applications. *Mater. Today* **2016**, *19* (4), 197−212.
(39) Nicholl, R. J. T.; Conley, H. J.; Lavrik, N. V.; Vlassiouk, I.; Puzyrev, Y. S.; Sreenivas, V. P.; Pantelides, S. T.; Bolotin, K. I. The effect of intrinsic crumpling on the mechanics of free-standing graphene. *Nat. Commun.* **2015**, *6* (1), 8789.
(40) Jung, G.; Qin, Z.; Buehler, M. J. Molecular mechanics of polycrystalline graphene with enhanced fracture toughness. *Extreme Mechanics Letters* **2015**, *2*, 52−59.
(41) Tavakoli, M. M.; Azzellino, G.; Hempel, M.; Lu, A.-Y.; Martin-Martinez, F. J.; Zhao, J.; Yeo, J.; Palacios, T.; Buehler, M. J.; Kong, J. Synergistic Roll-to-Roll Transfer and Doping of CVD-Graphene Using Parylene for Ambient-Stable and Ultra-Lightweight Photovoltaics. *Adv. Funct. Mater.* **2020**, *30* (31), 2001924.

https://doi.org/10.1021/acsapm.1c01328
ACS Appl. Polym. Mater. 2022, 4, 394−402